

Multifrequency VLA observations of the FRI radio galaxy 3C 31: morphology, spectrum and magnetic field

R.A. Laing ^{*1}, A.H. Bridle ², P. Parma ³, L. Feretti ³, G. Giovannini ^{3,4},
M. Murgia ^{3,5}, R.A. Perley ⁶

¹ *European Southern Observatory, Karl-Schwarzschild-Straße 2, D-85748 Garching-bei-München, Germany*

² *National Radio Astronomy Observatory, Edgemont Road, Charlottesville, VA 22903-2475, U.S.A.*

³ *INAF - Istituto di Radioastronomia, via Gobetti 101, I-40129 Bologna, Italy*

⁴ *Dipartimento di Astronomia, Università di Bologna, Via Ranzani, 1, I-40127 Bologna, Italy*

⁵ *INAF - Osservatorio Astronomico di Cagliari, Loc. Poggio dei Pini, Strada 54, I-09012 Capoterra (CA), Italy*

⁶ *National Radio Astronomy Observatory, P.O. Box O, Socorro, NM 87801, U.S.A.*

Received

ABSTRACT

We present high-quality Very Large Array (VLA) images of the Fanaroff & Riley Class I radio galaxy 3C 31 in the frequency range 1365 to 8440 MHz with angular resolutions from 0.25 to 40 arcsec. Our new images reveal complex, well resolved filamentary substructure in the radio jets and tails. We also use these images to explore the spectral structure of 3C 31 on large and small scales.

We infer the apparent magnetic field structure by correcting for Faraday rotation. Some of the intensity substructure in the jets is clearly related to structure in their apparent magnetic field: there are arcs of emission where the degree of linear polarization increases, with the apparent magnetic field parallel to the ridges of the arcs.

The spectra of the jets between 1365 and 8440 MHz are consistent with power laws within 60 arcsec of the nucleus. The spectral indices, α (flux density $\propto \nu^{-\alpha}$) are significantly steeper ($\alpha = 0.62$) within ≈ 7 arcsec of the nucleus than between 7 and 50 arcsec ($\alpha = 0.52 - 0.57$). The spectra of the arcs and of the jet edges are also slightly flatter than the average for their surroundings. At larger distances, the jets are clearly delimited from surrounding larger-scale emission both by their flatter radio spectra and by sharp brightness gradients.

The spectral index of 0.62 in the first 7 arcsec of 3C 31's jets is very close to that found in other FRI galaxies where their jets first brighten in the radio and where X-ray synchrotron emission is most prominent. Farther from the nucleus, where the spectra flatten, X-ray emission is fainter relative to the radio. The brightest X-ray emission from FRI jets is therefore not associated with the flattest radio spectra, but with a particle-acceleration process whose characteristic energy index is $2\alpha + 1 = 2.24$. The spectral flattening with distance from the nucleus occurs where our relativistic jet models require deceleration, and the flatter-spectra at the jet edges may be associated with transverse velocity shear.

Key words: galaxies: jets – radio continuum:galaxies – magnetic fields – polarization – MHD – acceleration of particles

1 INTRODUCTION

The radio galaxy 3C 31 is a nearby member of the low-luminosity FRI (Fanaroff & Riley 1974) class. Its prominent, symmetrical twin radio jets were discovered by Burch (1977) and imaged at higher resolution by Fomalont et al. (1980). The jets are asymmetric on scales up to ≈ 10 kpc and

only the brighter jet is detected on parsec scales (Lara et al. 1997). More diffuse tails of emission (Strom et al. 1983; Jägers 1987) extend for ≈ 20 arcmin on either side of the nucleus. The source shows strong linear polarization and a pronounced depolarization asymmetry (Burch 1979; Strom et al. 1983).

The detection of the brighter jet at optical wavelengths by Butcher, van Breugel & Miley (1980) was not confirmed by Fraix-Burnet, Golombek & Macchetto (1991)

* E-mail: rlaing@eso.org

or Keel (1988), but Croston et al. (2003) presented evidence for associated optical emission between 5 and 10 arcsec from the nucleus. X-ray emission from this jet was found by Hardcastle et al. (2002).

3C 31 is identified with the bright elliptical galaxy NGC 383, which we take to have a redshift of 0.0169 (the mean value from Smith et al. 2000, Huchra, Vogeley & Geller 1999 and De Vaucouleurs et al. 1991). NGC 383 is the brightest member of a rich group of galaxies (Arp 1966; Zwicky & Kowal 1968) and, in common with other nearby radio galaxies, has a dusty nucleus (Martel et al. 1999). Hot gas on group and galactic scales has been detected by X-ray imaging (Komossa & Böhringer 1999; Hardcastle et al. 2002).

Deep 8440-MHz Very Large Array (VLA) images of 3C 31 at resolutions of 0.75 and 0.25 arcsec were made by Laing & Bridle (2002a). They showed that the total intensity and linear polarization within 30 arcsec of the nucleus can be modelled on the assumption that the jets are intrinsically symmetrical, axisymmetric, relativistic and decelerating. They also assumed that the jet flows are stationary, in the sense that they are characterized by the same global parameters at all times. By fitting parameterized models of the velocity field, emissivity and field-ordering, they were able to deduce that the angle to the line of sight is $\approx 52^\circ$, to quantify the deceleration and to establish that transverse velocity gradients must be present in the jets. Laing & Bridle (2002b) used this kinematic model and a description of the external gas pressure and density from Hardcastle et al. (2002) to make a conservation-law analysis. They showed that the inferred velocity field is consistent with jet deceleration by entrainment of thermal matter and deduced the energy flux and the variations of pressure, density and entrainment rate with distance from the nucleus. Laing & Bridle (2004) examined adiabatic models for the jets in 3C 31: these models predict too steep a brightness decline along the jets for plausible variations of the jet velocity and fail to reproduce the observed magnetic-field structures.

In this paper we describe VLA observations of 3C 31 obtained under NRAO observing proposals AF236 and AL405 at frequencies between 1365 and 8440 MHz and resolutions of 0.25 – 40 arcsec (the 8440-MHz observations are those presented by Laing & Bridle 2002a). We then discuss three aspects of the astrophysics of 3C 31 which complement the treatment of its inner jet dynamics by Laing & Bridle (2002a,b, 2004) as follows.

(i) *Arcs and filaments.* The jets in 3C 31 contain discrete features – arcs and non-axisymmetric knots – visible in both total and linearly polarized intensity. Such features, and filamentation in general, are common in extragalactic synchrotron sources when observed with sufficiently high resolution and good spatial frequency coverage. In particular, Laing et al. (2006b) found similar arc-like structure in the twin-jet source 3C 296 and suggested that systematic differences between the arcs in the main (brighter) and counter-jets could also be a manifestation of differential relativistic aberration. In 3C 31, we study how the intensity gradients in such features are related to their magnetic-field structures.

(ii) *Large-scale spectral structure.* 3C 31 belongs to the sub-class of FRI sources with tails of diffuse emission extending away from the nucleus (as opposed to lobes with

well-defined outer edges). As in other members of the class (Parma et al. 1999), its radio spectrum steepens with distance from the nucleus (Burch 1977; Strom et al. 1983; Andernach et al. 1992). Analyses of such spectral variations from low-resolution observations (as made for 3C 31 by Andernach et al. 1992) interpreted them as the results of radiative losses on an energy spectrum initially of power-law form and derived corresponding time-scales, which were identified with dynamical ages. More recently, high-resolution observations (Katz-Stone & Rudnick 1997; Katz-Stone et al. 1999) have shown that spectral structures of a number of FRI sources are better described as a flat-spectrum ‘spine’ surrounded by a steeper-spectrum ‘sheath’ rather than as a single component whose spectrum varies smoothly with distance from the nucleus. In 3C 31, we have good spatial resolution over a range of frequencies and can examine the spectral variations in more detail.

(iii) *Jet base spectra, X-ray emission and particle acceleration processes.* We have recently shown that accurate imaging of radio spectra in FRI jet bases can reveal correlations between spectral index, X-ray emission and the jet kinematics as inferred from our relativistic models (Laing et al. 2006a,b). The shortness of the synchrotron lifetimes for electrons radiating in the X-ray band requires them to be accelerated in situ, so there must be a direct connection between the radio spectral index and the particle acceleration process. For 3C 31 we can determine the radio spectrum very accurately at high resolution and examine the connection with X-ray emission and kinematics in greater detail.

The observations and their reduction are described in Section 2 and the images are presented in Section 3. Discrete features in total intensity and the apparent magnetic-field structure are discussed in Section 4 and variations in radio spectrum across the source are described in Section 5. Section 6 summarizes our main conclusions. Faraday rotation and depolarization of the polarized emission are analysed in a companion paper (Laing et al. 2008) which discusses the structure of the magnetic field in the foreground screen that is responsible for the Faraday rotation measure (RM) fluctuations.

We assume a concordance cosmology with a Hubble Constant $H_0 = 70 \text{ km s}^{-1} \text{ Mpc}^{-1}$, $\Omega_\Lambda = 0.7$ and $\Omega_M = 0.3$. At the redshift of NGC 383 ($z = 0.0169$), this gives a linear scale of 0.344 kpc/arcsec. We also adopt the sign convention $S(\nu) \propto \nu^{-\alpha}$ for the spectral index, α .

2 OBSERVATIONS AND DATA REDUCTION

2.1 Observations

The observations were made with the NRAO VLA at frequencies between 1365 and 8440 MHz and in all four configurations of the array. A journal of observations is given in Table 1. The flux-density scale was set using observations of 3C 48 or 3C 286 and the zero-point of **E**-vector position angle with reference to 3C 138 or 3C 286. A single pointing centre (coincident with the galaxy nucleus) was used for all observations.

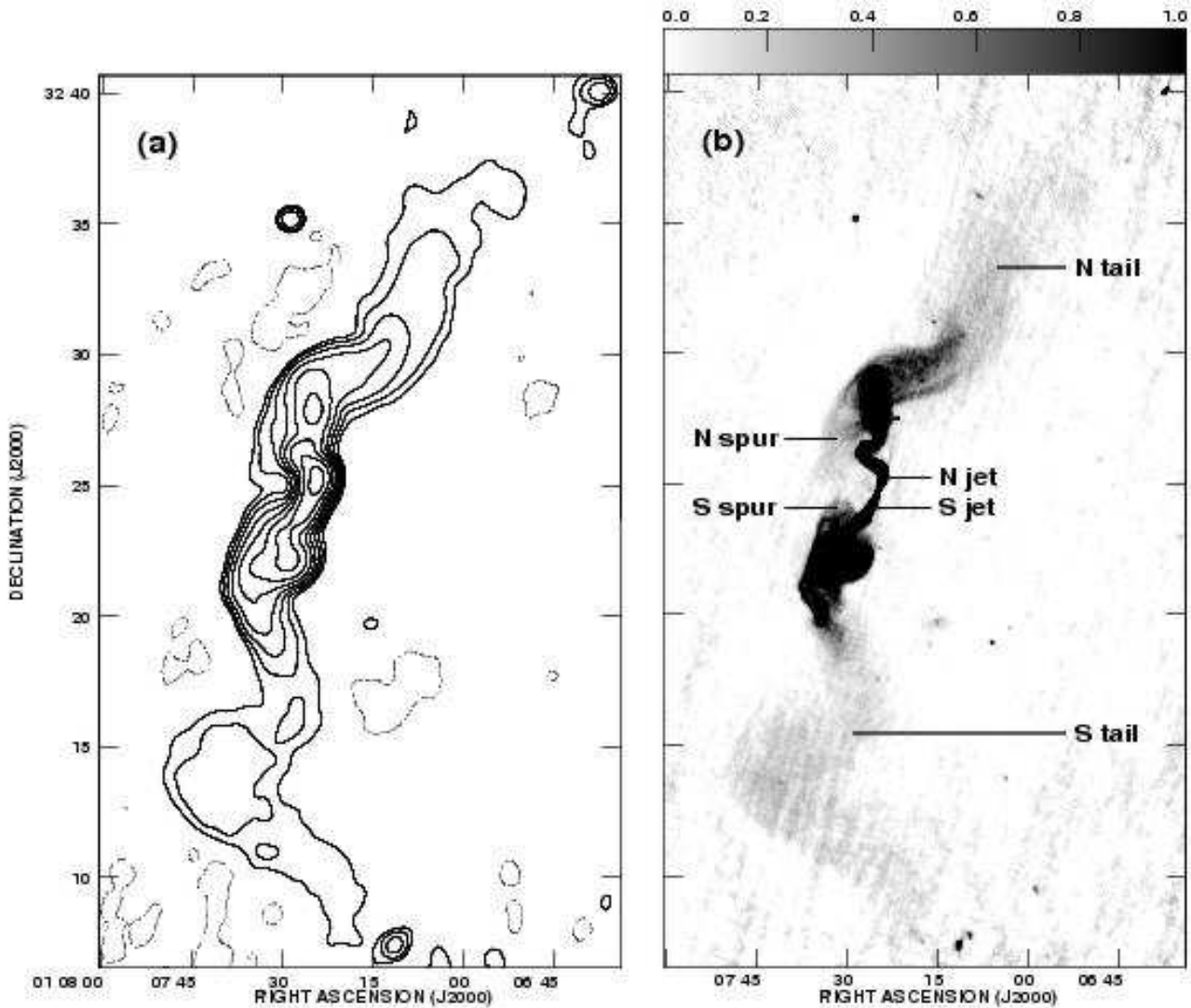


Figure 1. Low-resolution, mean L-band images (Section 2.2) optimized to show the extent of the observed large-scale structure. (a) Contours at 40 arcsec FWHM. The levels are $-1, 1, 2, 4, 8, 16, 32, 64, 128 \times 3.5 \text{ mJy beam}^{-1}$. (b) Grey-scale at 5.5 arcsec FWHM. The displayed range is $0 - 1 \text{ mJy beam}^{-1}$. Key regions are labelled, as discussed in the text. Note that the primary beam correction leads to increased noise at the edges of the field and that the low-level stripes in the tails (panel b) are artefacts. Chromatic aberration is large at the edges of panel (b), so images of point-like sources are smeared radially by a factor ≈ 3 and reduced in peak flux density by the same amount. The effect on the brightness distribution of 3C 31, which is fully resolved on these scales, is slight (Section 2.2).

2.2 Data reduction

Calibration and imaging of the VLA data were done using the AIPS software package and followed standard procedures with one exception: we used the iterative technique described by Laing & Bridle (2002a) in order to correct for core variations and amplitude errors when combining data from different configurations at 4985 and 8440 MHz. For the lower-frequency observations, core variability was below the level we could measure and no corrections were made.

We used both CLEAN and maximum entropy deconvolution methods for the total-intensity images and compared the results (in the latter case, we subtracted the core before deconvolution and restored it again afterwards). In all cases, the differences between the images (after convolution with the same Gaussian restoring beam) were less than the larger of $3\sigma_I$ (Table 2) and $0.01I$. The mean levels were consistent

to $\ll \sigma_I$ and the total flux densities differed by $< 1\%$. As usual, the maximum entropy images of extended, uniform brightness distributions were locally smoother and showed little of the patchy structure or high-frequency ripples characteristic of the CLEAN algorithm. We therefore show the maximum-entropy I images at resolutions of ≤ 1.5 arcsec. All quantitative measurements have also been checked on the CLEAN images.

The parameters of the images used in this paper are summarized in Table 2. All of the images have been corrected for the effects of primary beam attenuation: as a consequence, the quoted rms noise levels strictly refer to off-source regions close to the pointing centre. We have used the mean of the images at 1365, 1435, 1485 and 1636 MHz to provide several of the illustrations, and we refer to these as ‘mean L-band images’ (using the radio vernacular for des-

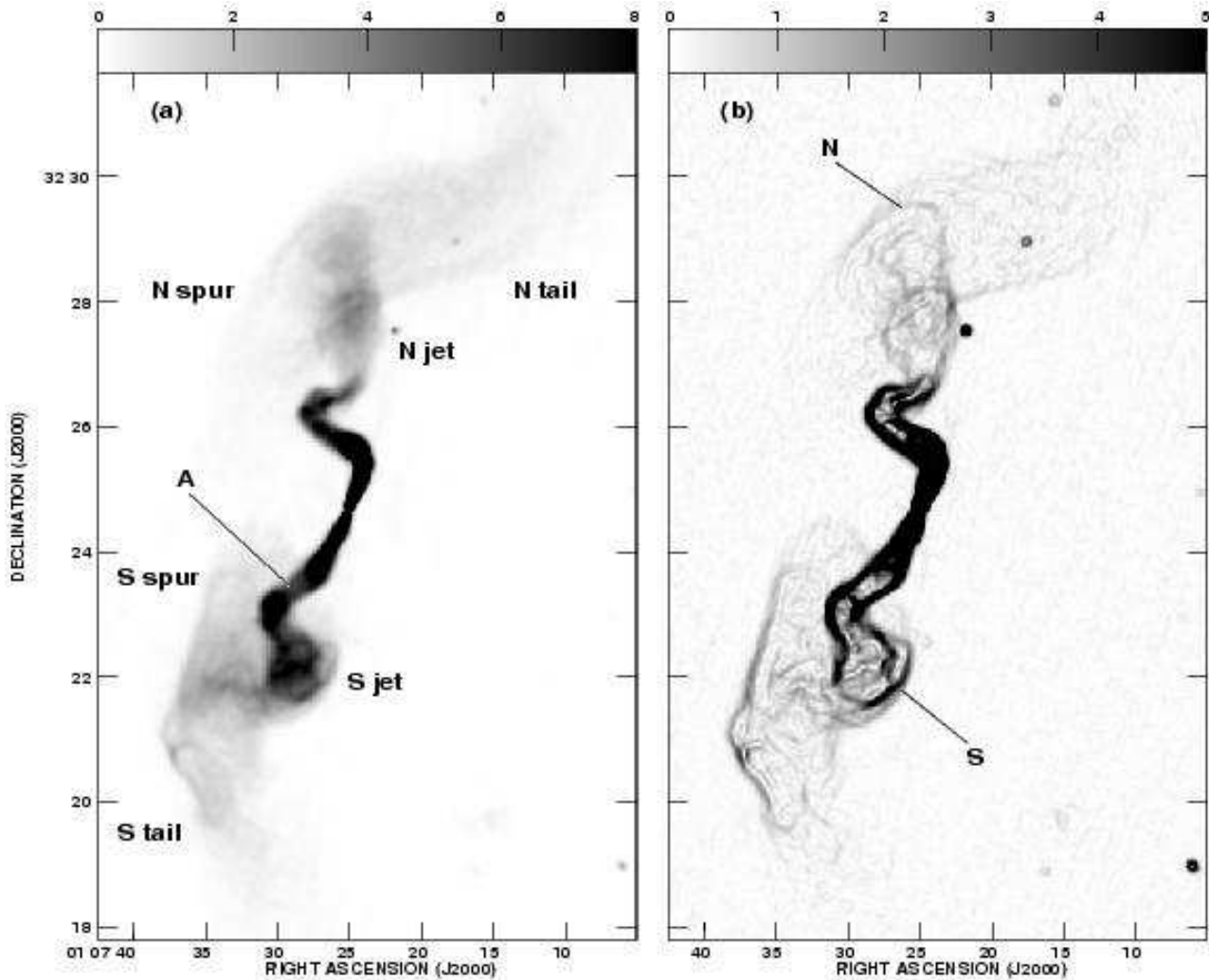


Figure 2. Grey-scale representations of the mean L-band image of 3C31 (Section 2.2) at a resolution of 5.5 arcsec FWHM. (a) Total intensity. The grey-scale range runs from 0 – 8 mJy beam⁻¹. (b) A Sobel-filtered version of the same image, normalized by the total intensity (see text).

ignation of this frequency band). We have checked the registration of the images at different frequencies using the peak of the core emission and isolated point sources in the field. We believe that the images at 1.5 and 5.5 arcsec FWHM are aligned to better than FWHM/20.

The effects of limited short-spacing coverage and primary beam attenuation are important at the two highest frequencies, particularly for spectral analysis. We estimate that the 4985-MHz and 8440-MHz images are adequately sampled for scales $\lesssim 300$ arcsec and $\lesssim 140$ arcsec, respectively, i.e. ± 150 and ± 70 arcsec from the nucleus (Taylor, Ulvestad & Perley 2003). There is less power on large spatial scales in Q and U , and we estimate that these are reliable at significantly larger distances from the nucleus.

Chromatic aberration (“bandwidth smearing”) causes point-like sources far from the phase centre to appear distorted and reduced in peak flux density. This effect is large at the periphery of our 5.5-arcsec L-band images (Fig. 1b) and typically causes a loss of peak intensity of 5 – 10% for point sources at the edges of the areas we show in the remaining figures (Taylor, Ulvestad & Perley 2003). Chromatic aber-

ration preserves flux density, however, and 3C 31 is fully resolved on all scales where it is significant. Its effect on the images of the source shown in this paper is therefore very small compared with other errors. A 10-s integration time was used for all of the observations, so time-average smearing is negligible over all of our fields (Taylor, Ulvestad & Perley 2003).

When deriving images of polarized power, $P = (Q^2 + U^2)^{1/2}$, and degree of polarization $p = P/I$, we made a first-order correction for Ricean bias (Wardle & Kronberg 1974).

3 THE IMAGES

3.1 Large-scale structure

Fig. 1 shows the large-scale structure of 3C 31. The 40-arcsec FWHM image (Fig. 1a) shows the maximum detectable extent of the structure at high signal/noise ratio. The lowest contour is essentially identical to that seen in previous low-frequency images (Burch 1977; Strom et al. 1983; Jägers 1987; Andernach et al. 1992).

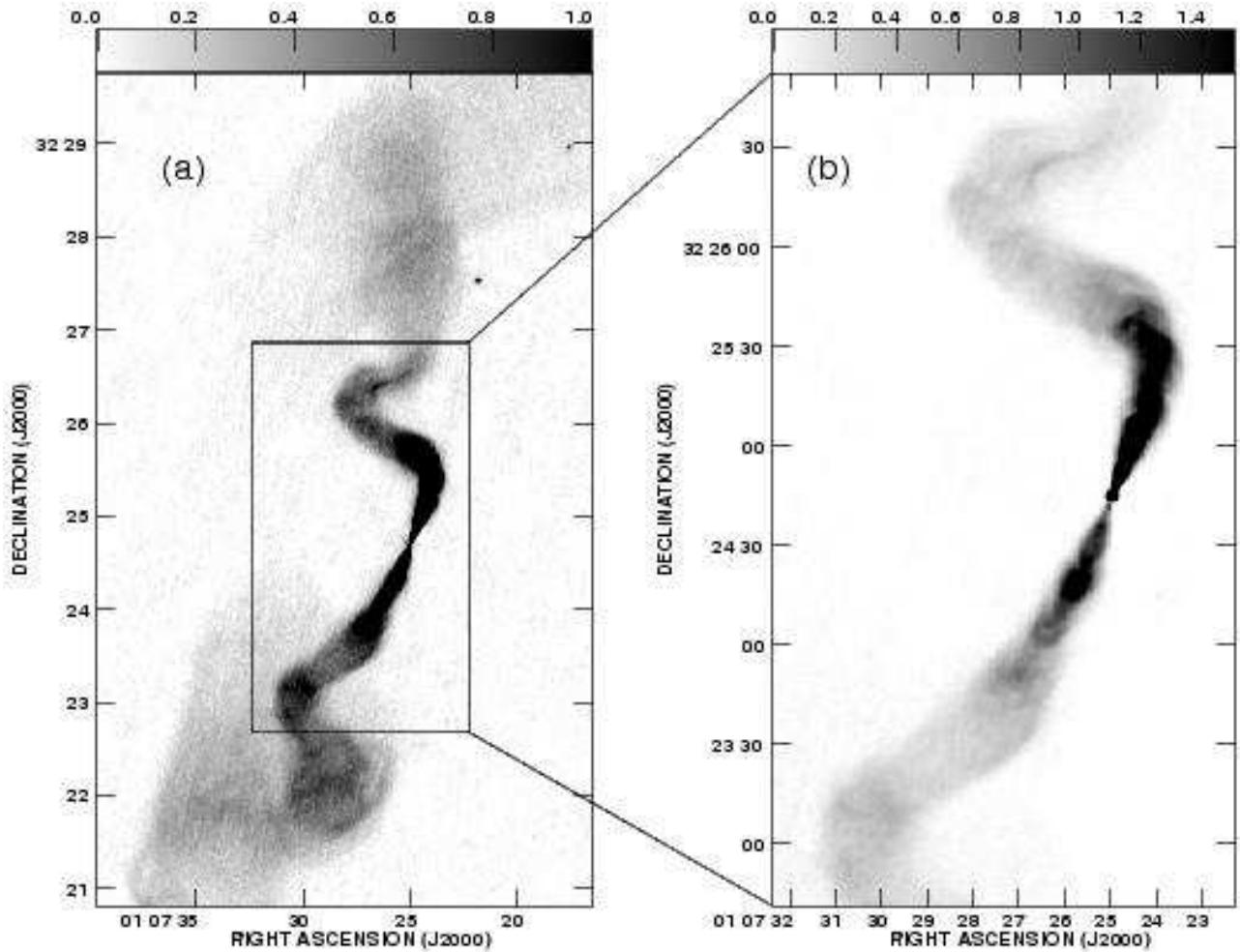


Figure 3. Grey-scale images of 3C31 at a resolution of 1.5 arcsec FWHM. (a) Mean L-band maximum-entropy deconvolution (Section 2.2), 0 – 1 mJy beam⁻¹. (b) 4985 MHz maximum entropy deconvolution, 0 – 1.5 mJy beam⁻¹. The area covered by (b) is shown by the box on (a).

In Fig. 1(b), we show a grey-scale representation of the mean L-band image at a resolution of 5.5 arcsec FWHM, over a flux-density range chosen to emphasise the low-brightness structure. All of the emission visible at lower resolution is seen on this image, albeit at a lower level of significance and with some artefacts. Key regions of the source are labelled: we refer to North and South *jets*, *spurs* and *tails*. The essential distinction between tails and spurs is that the former extend away from the nucleus whereas the latter extend back towards it, at least in projection. Filamentation and fine structure are already apparent in Fig. 1(b): the bifurcation of the North tail and the filaments in the North spur are best seen on this display. The remarkably straight East edge of the South spur is more prominent than on earlier images.

In a display of the mean L-band image at 5.5 arcsec FWHM resolution over a larger intensity range (Fig. 2a), the true extent of the jets becomes apparent. In order to display the intensity gradients more clearly, we show a Sobel-filtered representation of the image in Fig. 2(b). The Sobel operator (Pratt 1991) computes $|\nabla I|$ and therefore enhances brightness gradients. We show an image of fractional intensity gradient $|\nabla I|/I$. This image shows that the boundaries

of the jets are marked by strong fractional intensity gradients. These can be followed to the positions marked N and S in Fig. 2(b) and we therefore use them to define the boundaries of the jet, spur and tail regions. At the points N and S, there is evidence for curved features with sharp brightness gradients slightly inside the outer boundary of the source. It is tempting to associate these features with the redirection of the jets to form the tails and spurs. It may also be that the spur and tail are parts of the same physical structure, seen in projection on either side of the jet.

The South jet has a well-collimated region of comparatively low emissivity (labelled ‘A’ in Fig. 2a) which begins where it becomes superposed on the spur. Thereafter it bends through $\approx 90^\circ$ and brightens before widening and appearing to merge with the spur and tail emission. The North jet makes a sharp double bend before widening. Both jets show complex, but well-resolved sub-structure after they widen. This sub-structure is clearly evident in Fig. 2(a), but is not prominent in the fractional intensity gradient image (Fig. 2b). The straight edge in the South spur noted earlier is particularly prominent on the Sobel-filtered image (Fig. 2b).

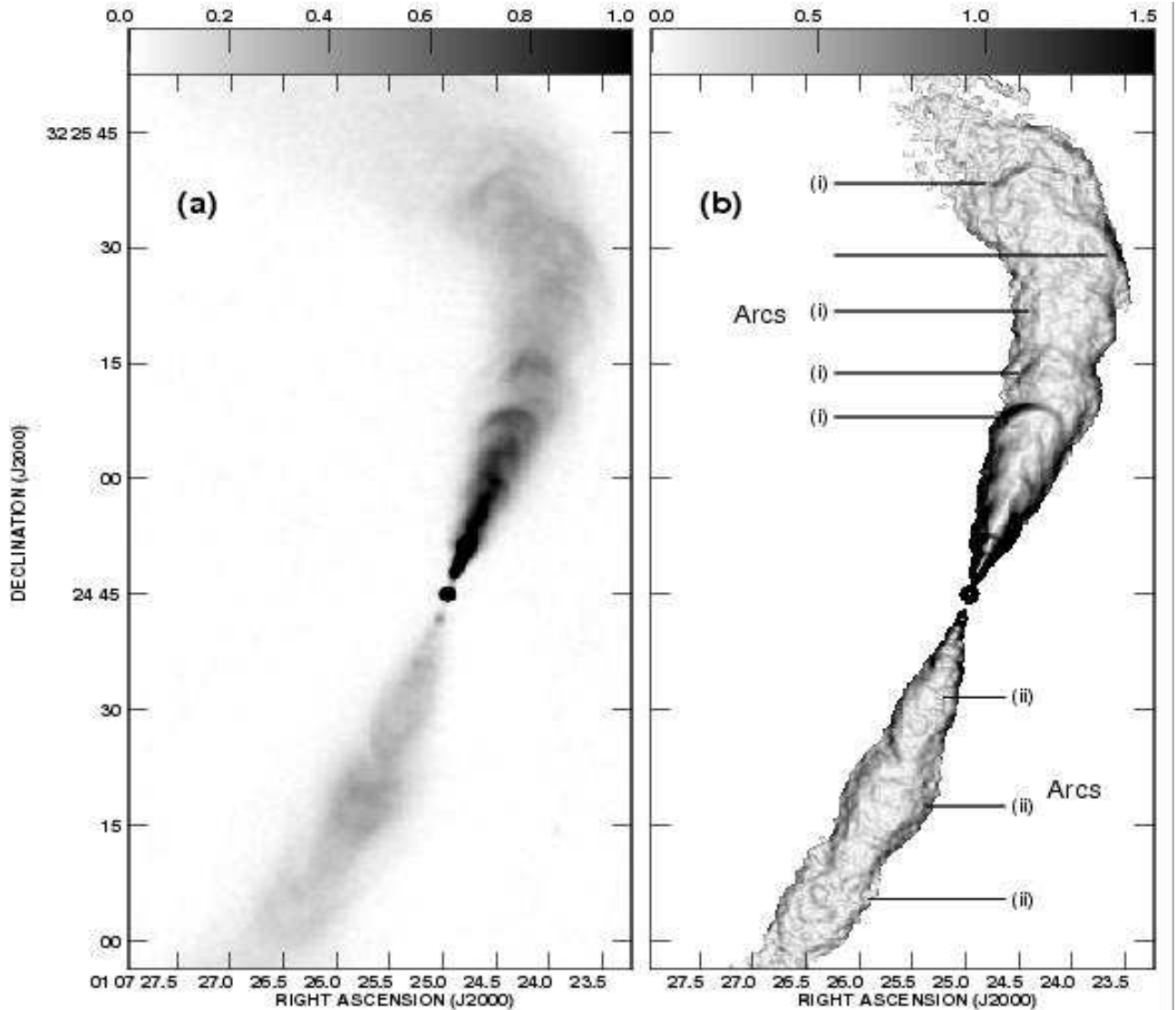


Figure 4. Grey-scale image of 3C31 observed at 8440 MHz with a resolution of 0.75 arcsec FWHM. (a) Total intensity ($0 - 1 \text{ mJy beam}^{-1}$). (b) Sobel-filtered and normalized by total intensity. The ‘arcs’ discussed in Section 3.3 are indicated and labelled with their morphological types where these can be ascertained.

3.2 Total intensity images at 1.5 arcsec resolution

A clearer representation of the termination of the jets is given by the mean L-band image at 1.5-arcsec FWHM resolution (Fig. 3a), in which the tail emission is heavily resolved. The internal structure of the jets starts to be revealed by the 4985-MHz image at the same resolution (Fig. 3b). The main new features are as follows:

- (i) There is evidence for considerable filamentation and other sub-structure within both jets. We discuss this in detail below (Sections 3.3 and 4.2).
- (ii) The low-emissivity region A of the South jet mentioned earlier is seen in more detail. It appears to narrow slightly before bending and brightening.
- (iii) The region where the South jet expands inside the South tail shows complex, resolved filamentary fine structure.

3.3 8440 MHz total intensity images at 0.75 and 0.25 arcsec resolution

The higher-resolution images shown here cover a wider area than those discussed by Laing & Bridle (2002a). The 0.75-arcsec FWHM image (Fig. 4a) shows a number of features with sharp intensity gradients. Examples of these ‘arcs’ are labelled in Fig. 4(b) with their morphological types as defined by Laing et al. (2006b). In order to display them more clearly, Fig. 5 shows the relevant areas of the North and South jets on an expanded scale and with a narrower grey-scale range. The main characteristics of the arcs are as follows.

- (i) The most prominent examples are at distances $\gtrsim 20 \text{ arcsec}$ (7 kpc) from the nucleus, but there are hints of similar structures closer in.
- (ii) They all start from an edge of the jet and extend

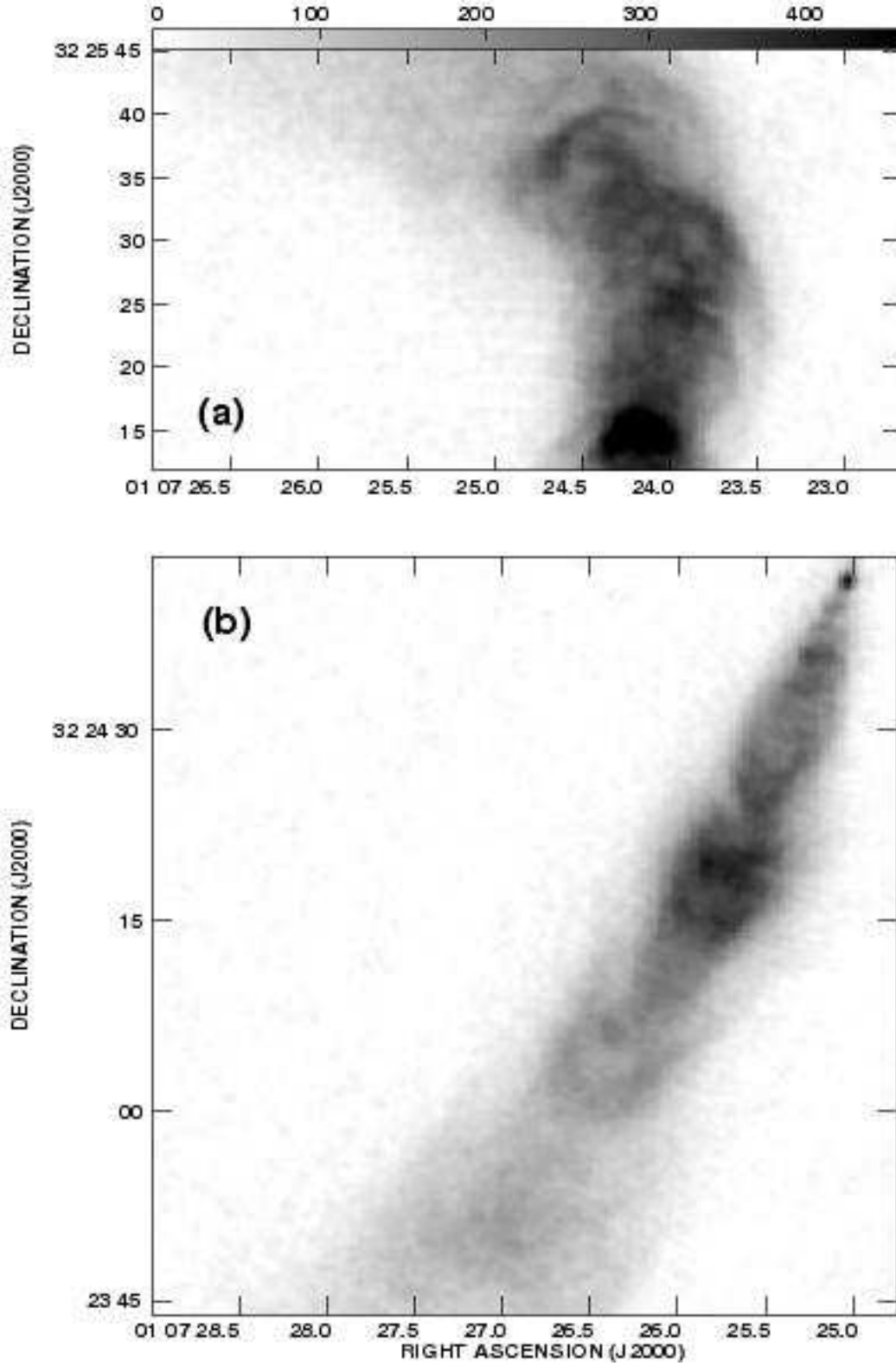


Figure 5. Grey-scale images of 3C31 observed at 8440 MHz with a resolution of 0.75 arcsec FWHM. The grey-scale range is 0 – 0.5 mJy beam⁻¹. (a) North jet, around the first bend; (b) South jet (note that the nucleus is not included in this panel).

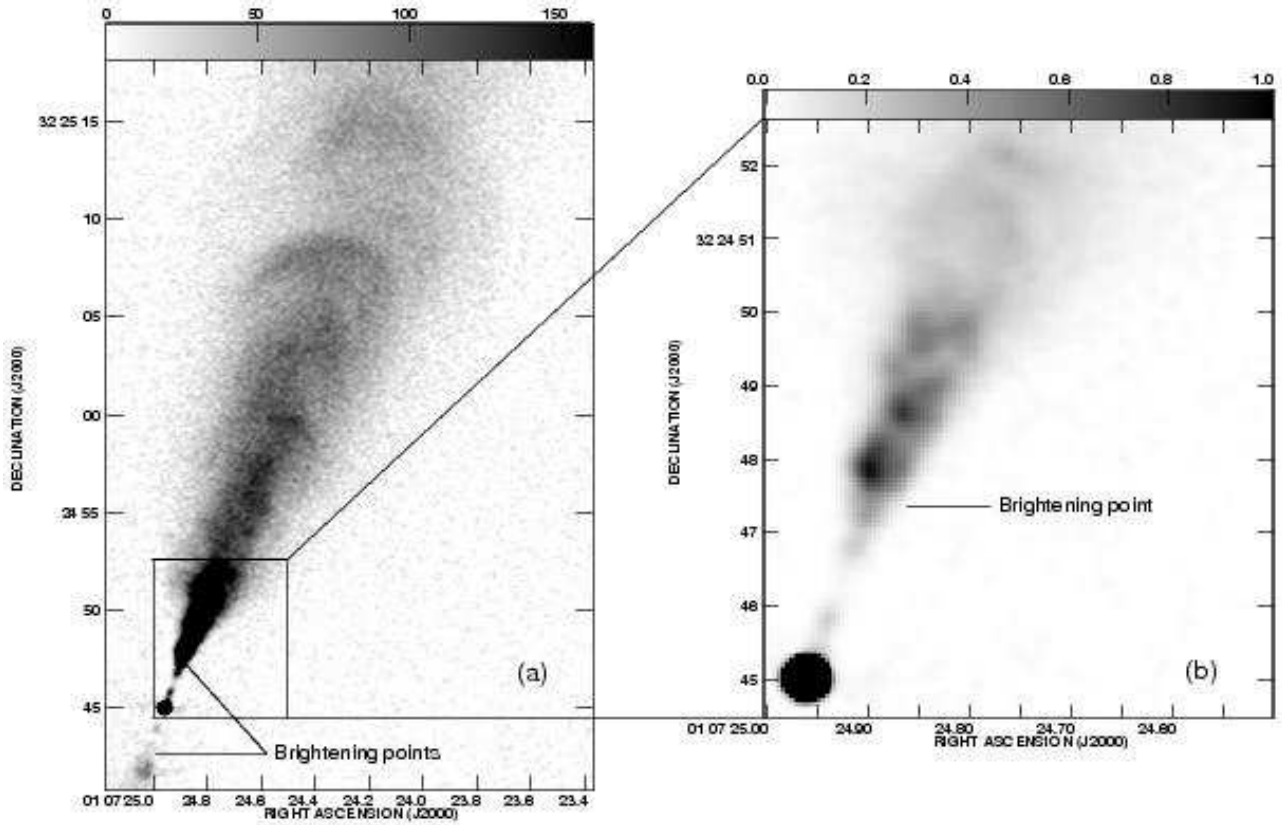


Figure 6. Grey-scale images of 3C31 observed at 8440 MHz with a resolution of 0.25 arcsec FWHM. The grey-scale ranges for the two panels are: (a) 0 – 160 $\mu\text{Jy beam}^{-1}$; (b) 0 – 1 mJy beam^{-1} . The box on panel (a) shows the area covered by (b).

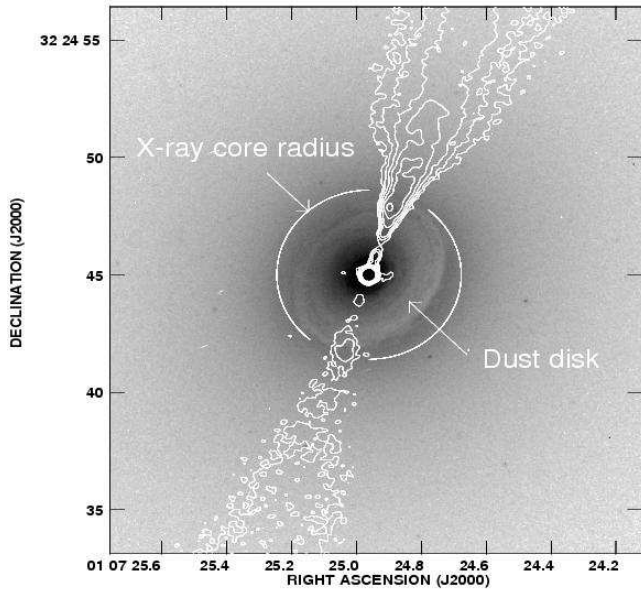


Figure 7. Grey-scale of optical emission near 7000 Å observed with HST WFPC-2, superimposed on contours of total intensity at 8440 MHz with 0.25 arcsec FWHM resolution. The location of the dust disk and the core radius of the inner hot gas component are marked (Martel et al. 1999; Hardcastle et al. 2002).

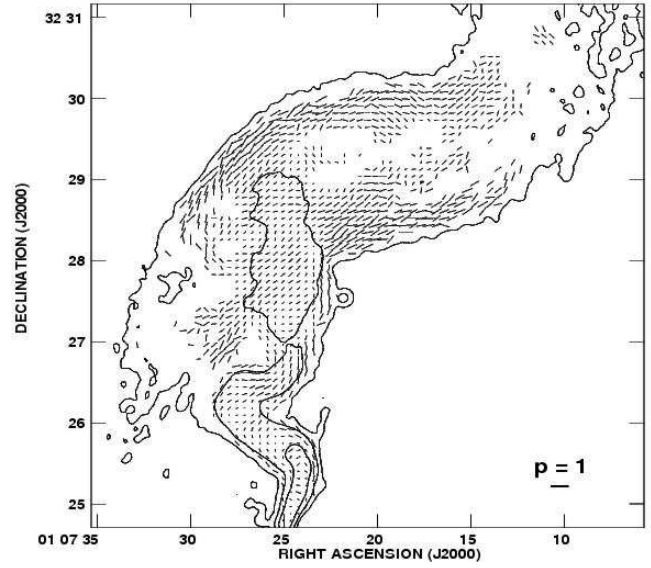


Figure 8. Vectors whose lengths are proportional to the mean degree of polarization, p , at L-band and whose position angles represent the apparent magnetic field direction, $\chi(0) + \pi/2$, where $\chi(0)$ is the zero-wavelength \mathbf{E} -vector position angle from a rotation-measure fit to all four L-band frequencies (Laing et al. 2008). The resolution is 5.5 arcsec FWHM and the polarization scale is indicated by the labelled bar. The diagram is designed to show the magnetic-field structure in the North tail over a region which is not sampled by the 4985- and 8440-MHz observations.

Table 1. Journal of observations. The columns are: (1) VLA configuration, (2) centre frequency, (3) bandwidth, (4) date of observation and (5) integration time.

| Conf | ν MHz | $\Delta\nu$ MHz | Date | t min |
|------------------|-------------------|--------------------|-------------|----------|
| A | 8460 ^a | 100.00 | 1996 Nov 12 | 606 |
| | 1636 | 6.25 | 1995 Apr 28 | 192 |
| | 1485 | 6.25 | 1995 Apr 28 | 192 |
| | 1435 | 6.25 | 1995 Apr 28 | 192 |
| | 1365 | 6.25 | 1995 Apr 28 | 192 |
| A/B ^b | 8440 | 100.00 | 1994 Jun 6 | 406 |
| B | 8440 | 100.00 | 1994 Jun 14 | 412 |
| | 4985 | 50.00 | 1993 Feb 25 | 535 |
| | 1636 | 25.00 | 1994 Jun 13 | 192 |
| | 1485 | 25.00 | 1994 Jun 13 | 192 |
| | 1435 | 25.00 | 1994 Jun 13 | 192 |
| C | 1365 | 25.00 | 1994 Jun 13 | 192 |
| | 8440 | 100.00 | 1994 Dec 4 | 242 |
| | 4985 | 50.00 | 1994 Dec 4 | 165 |
| | 1636 | 25.00 | 1994 Nov 26 | 140 |
| | 1485 | 25.00 | 1994 Nov 26 | 140 |
| D | 1435 | 25.00 | 1994 Nov 26 | 139 |
| | 1365 | 25.00 | 1994 Nov 26 | 139 |
| | 8440 | 100.00 | 1995 Apr 28 | 69 |
| | 4985 | 50.00 | 1995 Apr 28 | 69 |
| | 1636 | 25.00 | 1995 Apr 28 | 61 |
| | 1485 | 25.00 | 1995 Apr 28 | 61 |
| | 1435 | 25.00 | 1995 Apr 28 | 69 |
| | 1365 | 25.00 | 1995 Apr 28 | 69 |

^a The slight difference in centre frequency used for the A-configuration observations has no measurable effect on the results and we refer throughout to the ‘8440-MHz observations’.

^b Most antennas were in the B configuration.

inwards towards the jet axis in the downstream direction (i.e. away from the nucleus).

(iii) The most prominent examples are narrow and ridge-like, but there are many fainter and broader features.

(iv) Three of the arcs in the North jet clearly cross the axis. They are concave towards the nucleus and approximately semi-circular in form [the defining characteristics of type (i) arcs given by Laing et al. (2006b)].

(v) The remaining arcs in the North jet have higher brightness contrast at the outside edge of the bend. It is possible that they also extend across most of the jet, but at lower contrast.

(vi) The features in the South jet have a greater degree of mirror symmetry across the jet and show similar brightness contrast on both sides. They are type (ii) arcs as defined by Laing et al. (2006b): oblique to the jet direction on either side of the jet but without large brightness gradients on-axis. They are located within the outer envelope of the jet emission, so the highest brightness gradients do not occur at the jet edges (Fig. 5b).

(vii) The maximum local brightness enhancement is

Table 2. Parameters of the images.

| ν MHz | FWHM arcsec | σ / $\mu\text{Jy beam}^{-1}$ I | QU |
|--------------|----------------|--|----|
| 8440 | 0.25 | 6 | 6 |
| 8440 | 0.75 | 7 | 6 |
| 8440 | 1.50 | 11 | 6 |
| 4985 | 1.50 | 12 | 12 |
| 1636 | 1.50 | 72 | 64 |
| 1485 | 1.50 | 73 | 66 |
| 1435 | 1.50 | 78 | 68 |
| 1365 | 1.50 | 76 | 62 |
| Mean L-band | 1.50 | 34 | — |
| 8440 | 5.50 | 37 | 12 |
| 4985 | 5.50 | 26 | 16 |
| 1636 | 5.50 | 61 | 22 |
| 1485 | 5.50 | 52 | 23 |
| 1435 | 5.50 | 68 | 25 |
| 1365 | 5.50 | 68 | 23 |
| Mean L-band | 5.50 | 39 | — |
| Mean L-band | 40.00 | 100 | — |

$\approx 40\%$ (for the brightest arc in the North jet); $\lesssim 20\%$ for the other arcs. The implied emissivity enhancements in the arcs would be of order 400% to 200%, *if* their depths along the line of sight are of the same order as their apparent widths.

We discuss the magnetic-field structure and other properties of the arcs in Section 4.2.

Finally, Fig. 6 shows the inner jet region at 0.25-arcsec resolution in two different grey-scale representations. Fig. 6(a) shows that the brightest arc in the North jet is fully resolved, with a characteristic width ≈ 1 arcsec. The Figure also displays the knot at the base of the counter-jet which marks the *brightening point* on that side of the nucleus (we model the brightening as a sudden increase in emissivity at 2.5 arcsec from the nucleus in projection on both sides; Laing & Bridle 2002a). Fig. 6(b) illustrates the non-axisymmetric knot structure at the base of the North jet.

3.4 Optical-radio superposition at high resolution

HST WFPC-2 observations of 3C 31 were presented by Martel et al. (1999), who showed that there is a complex central dust lane of radius ≈ 3 arcsec. A superposition of our 8440-MHz image at 0.25 arcsec FWHM resolution on the HST image is shown in Fig. 7. In order to correct for uncertainties in the relative astrometry, we assumed that the brightest points on the optical and radio images coincide. The orientation and size of the kpc-scale rotating molecular disk studied by Okuda et al. (2005) are consistent with those of the dust lane. The radio jet flares and brightens on approximately the same (projected) scale as significant substructure (banding) in the dusty molecular disk (Fig. 7), but the latter is grossly misaligned with the jet axis and

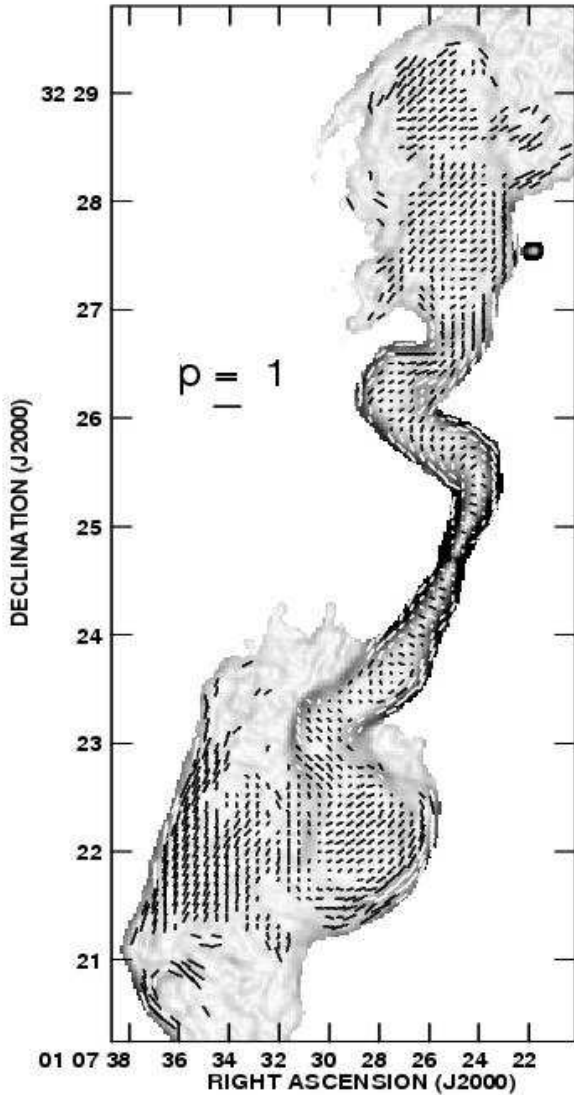


Figure 9. Vectors whose lengths are proportional to the mean degree of polarization, p , at 4985 MHz and whose position angles represent the apparent magnetic field direction, $\chi(0) + \pi/2$, where $\chi(0)$ is the zero-wavelength **E**-vector position angle from a rotation-measure fit to all frequencies between 1365 and 4985 MHz (see Laing et al. 2008, Fig.2c). The grey-scale is a Sobel-filtered, mean L-band image, normalized by total intensity. The resolution is 5.5 arcsec FWHM and the polarization scale is indicated by the labelled bar.

there is no evidence for any *direct* interaction between the two structures (de Koff et al. 2000). The flaring scale is also comparable with the core radius of the inner hot gas component identified by Hardcastle et al. (2002) and indicated on Fig. 7. We have argued elsewhere that the flaring and recollimation of the jets in 3C 31 is governed by the pressure of hot gas associated with the parent galaxy, rather than by interaction with the cool component (Laing & Bridle 2002b).

4 FIELD STRUCTURE AND INTENSITY GRADIENTS

We have estimated the degree of polarization at zero frequency, $p(0)$ and the direction of the apparent magnetic field ($\chi(0) + \pi/2$, where $\chi(0)$ is the zero-wavelength **E**-vector position angle) by correcting the observed values of p and the **E**-vector position angles for depolarization and Faraday rotation, respectively. The depolarization in the North of the source at 5.5-arcsec resolution and over the entire area visible at higher resolution is very small and the change of **E**-vector position angle is accurately proportional to λ^2 , so these corrections are well-determined (Laing et al. 2008). The rotation-measure distribution and its implications for the structure of the magnetoionic medium around 3C 31 are analysed in Laing et al. (2008); here we describe only the apparent field structure within the jets and its relation to features of their total intensity.

4.1 Field structure on large scales

Fig. 8 shows the apparent magnetic-field structure of the outer North jet, spur and tail derived from an L-band RM fit at 5.5 arcsec FWHM (see Laing et al. 2008, Fig. 2b). The degree of polarization is high ($p \approx 0.5 - 0.6$) at the edges of the North tail and spur. There is a clear polarization minimum in the centre of the tail, suggesting that the three-dimensional field configuration might be close to model B of Laing (1981), where the longitudinal and toroidal components are roughly equal but there is no field in the radial direction, perpendicular to the axis of the tail.

Fig. 9 shows the apparent magnetic-field structure at 5.5-arcsec resolution from a 5-frequency fit. The remarkable straight edge of the South spur is highly polarized at 4985 MHz, with an apparent field along the edge, suggesting that this part of the radio source has experienced compression or shear at a large-scale planar boundary whose counterpart in the surrounding gas has yet to be identified.

At 1.5-arcsec resolution (Fig. 10), the apparent field structure of the jets becomes clear. To a first approximation, the outer regions of both jets continue to show the configuration discussed in detail by Laing & Bridle (2002a) for the inner 30 arcsec – an apparent field which is transverse on-axis but longitudinal at the edges of the jets. In the North jet (Fig. 10b) this configuration persists for at least another 30 arcsec after the first bend. Thereafter, the on-axis field remains transverse, but there is insufficient sensitivity to measure the polarization at the jet edges. After the second bend, the apparent field becomes longitudinal over most of the jet. The degree of polarization is significantly enhanced at the outside edges of major bends in both jets. Where the South jet expands rapidly (Fig. 10a), it shows a predominantly transverse apparent field, again with high p . There is a highly-polarized edge where the jet makes its final sharp turn prior to disrupting at the feature S in Fig. 2.

The apparent magnetic field in the brighter jet at 0.25-arcsec resolution was shown by Laing & Bridle (2002a).

4.2 Magnetic fields in the arcs

A superposition of the Sobel-filtered, 0.75-arcsec FWHM *I* image and vectors showing the magnitude of p and the ap-

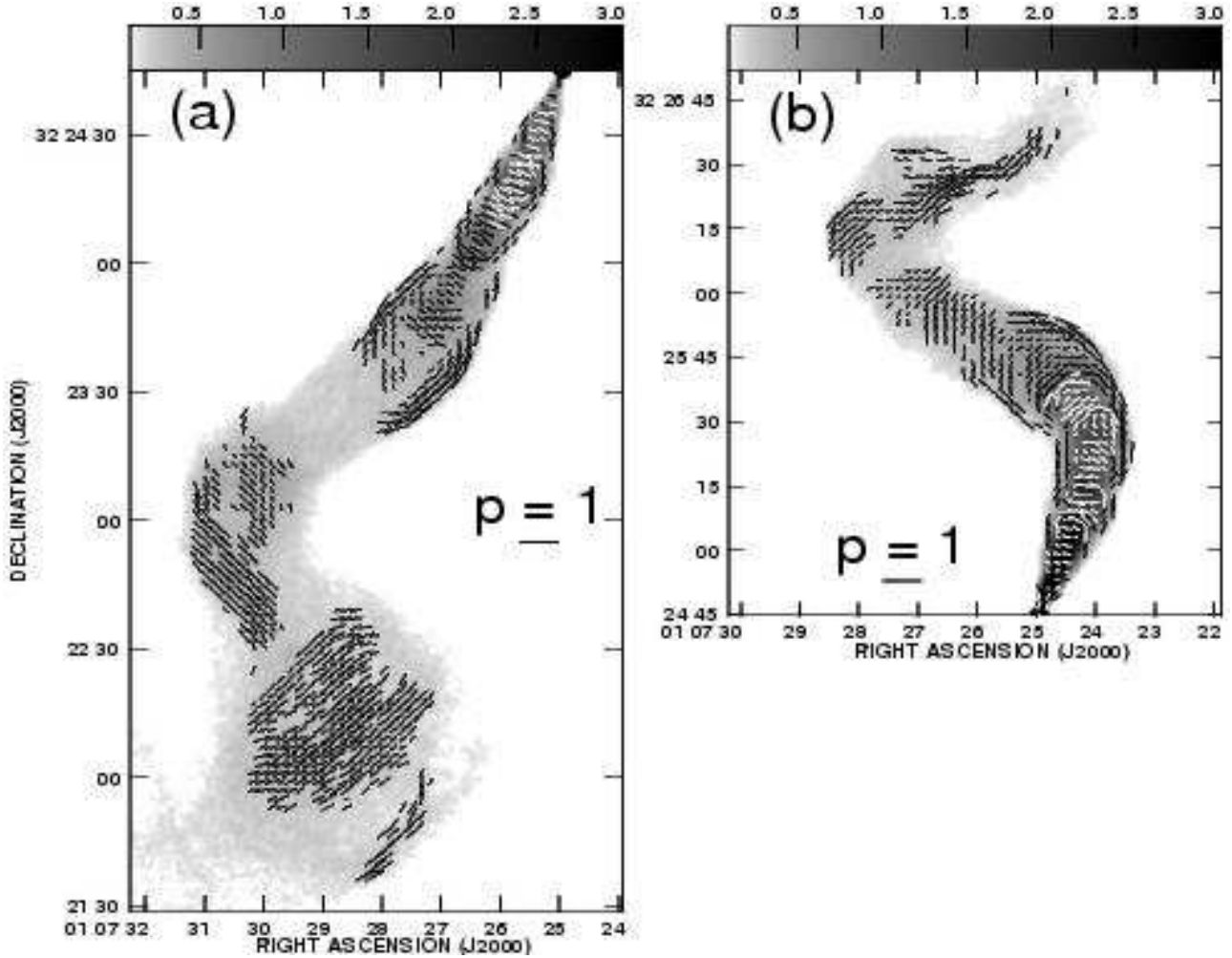


Figure 10. Vectors whose lengths are proportional to $p(0)$, the degree of polarization extrapolated to zero wavelength from a linear fit of p against λ^2 (Laing et al. 2008). Their angles represent the apparent magnetic field direction, $\chi(0) + \pi/2$, where $\chi(0)$ is the zero-wavelength **E**-vector position angle corresponding to the RM image of Laing et al. (2008, Fig. 3c). The vectors are superposed on a grey-scale of the 4985-MHz total intensity. The resolution is 1.5 arcsec FWHM and the polarization scale is indicated by the labelled bars. (a) South jet; (b) North jet.

parent field direction is shown in Fig. 11. This reveals two striking effects:

- (i) The polarization is enhanced wherever there is a strong gradient in total intensity, particularly at the arcs. For example, $p \approx 0.4$ in the brightest arc in the North jet, even without correction for contamination by surrounding emission.
- (ii) The apparent field always appears parallel to the arcs.

The arcs in 3C 296 show similar, but less prominent magnetic-field structures (Laing et al. 2006b).

In Laing et al. (2006b), we argued that the difference between type (i) arcs (found predominantly in the main jets) and type (ii) (usually in the counter-jets) was plausibly due to relativistic aberration. We suggested that a first-order model of an arc is a thin, axisymmetric shell of enhanced emissivity, concave towards the nucleus and travelling outward with approximately the velocity of the local mean flow. In that case, when our line of sight is tangential to part of the shell *in its rest frame*, we will see enhanced emission.

Close to the centre-line of the jet, the shell can be approximated as a planar sheet of material orthogonal to the axis in the rest frame of the flow. Relativistic aberration causes the sheets to appear differently orientated to the line of sight in the main and counter-jets so that those in the main jet can be observed nearly edge-on while those in the counter-jet are always significantly rotated about a line perpendicular to the jet axis in the plane of the sky and are therefore less prominent both in intensity and in brightness gradient where they cross the jet axis. These differences between the main jet and counter-jet are less pronounced for the slower flow at the edges of the jets, where the arcs can therefore appear more symmetrical – as observed. If the magnetic field in the arcs is compressed to lie in the plane of the shells, we also expect to see a high degree of polarization with the apparent field direction along the arc, as observed (Laing 1980).

The arcs therefore provide further support for the hypothesis that the main differences in appearance between the inner main jet and counter-jet in 3C 31 arise from rel-

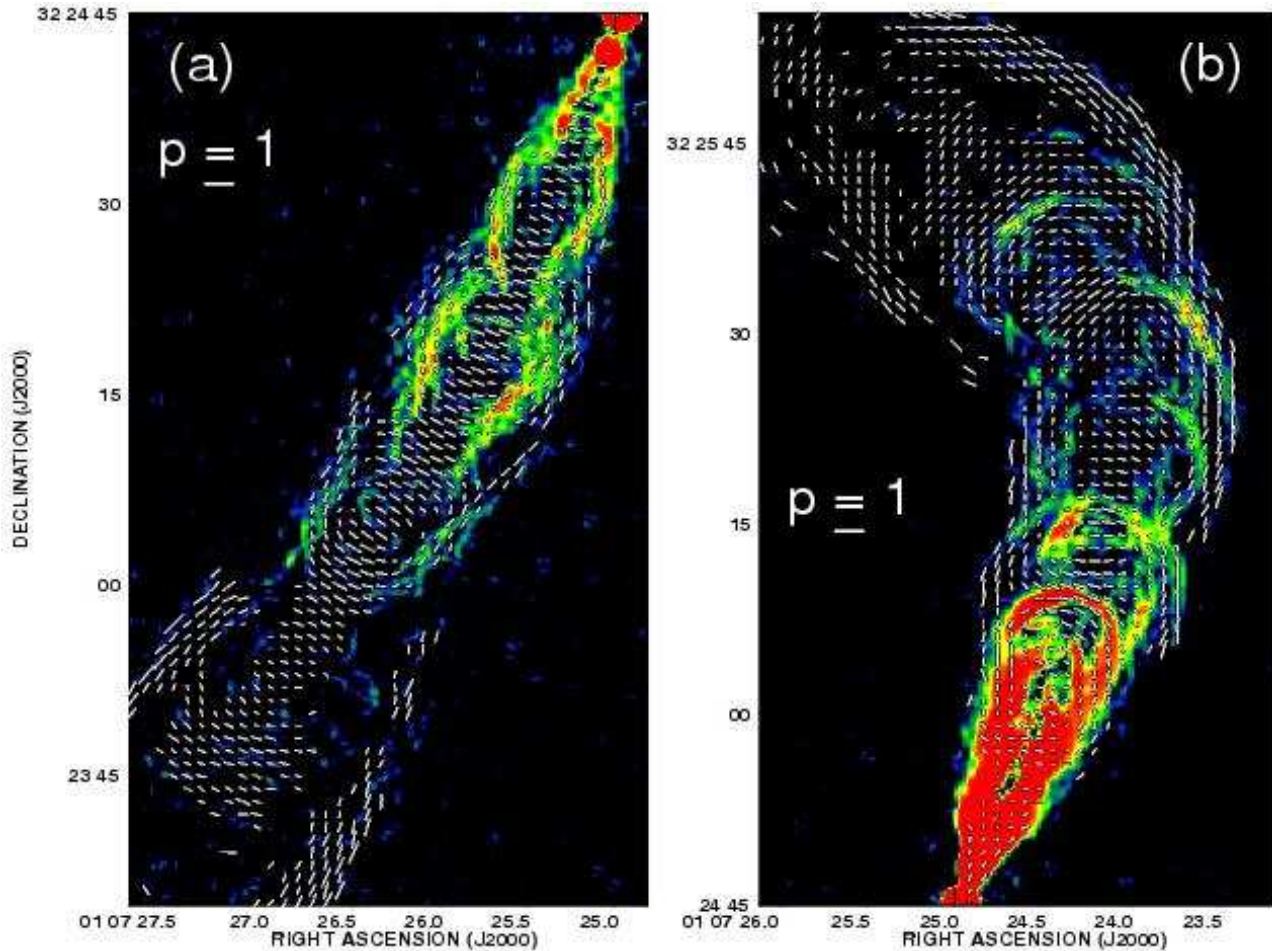


Figure 11. The colour plots show Sobel-filtered, 8440-MHz I images at a resolution of 0.75 arcsec FWHM superimposed on vectors whose magnitudes are proportional to the degree of polarization, p , and whose directions are those of the apparent magnetic field. The field directions were derived by interpolating the RM image of Laing et al. (2008, Fig. 3c) onto a finer grid and using it to correct the observed 8440-MHz E -vector position angles to zero wavelength. (a) South jet; (b) North jet.

ativistic bulk motion in intrinsically similar jet outflows on the two sides of the nucleus.

5 SPECTRA

5.1 Comparison of images at different frequencies

At 4985 and 8440 MHz, we cannot observe the full range of spatial frequencies covered by the D configuration at L band. We have therefore investigated the sensitivity of the spectral index determination between 1365 and 4985 MHz at 5.5 arcsec resolution to differences in the (u, v) coverage by comparing the spectral index distributions obtained from images made with:

- (i) all of the observed data at both frequencies, imaged with zero-spacing flux densities specified;
- (ii) matched coverage at the two frequencies, with the central portion of the (u, v) plane, including the zero spacing, deleted at 1365 MHz;
- (iii) as in (ii), but with the zero-spacing flux densities included.

We show results only for areas of 3C 31 where the spectral indices obtained by these three methods agree ($\Delta\alpha < 0.1$). The limitations in (u, v) coverage and primary beam size imply that we can derive reliable spectra only for the North and South jets and the South spur between 1365 and 4985 MHz at a resolution of 5.5 arcsec: the tails and the North spur are seen only at L-band, within which the range of observed frequencies is too small for us to derive reliable spectral indices.

Similar considerations apply at 1.5-arcsec resolution, where we have also compared spectral-index distributions derived from CLEAN and maximum-entropy deconvolutions. Spectra derived from the 8440-MHz images are reliable only within ± 70 arcsec of the nucleus, for the following reasons:

- (i) As mentioned earlier, the short-spacing coverage of the VLA D-configuration is inadequate to image structure on larger scales (Taylor, Ulvestad & Perley 2003).
- (ii) A comparison of spectral indices derived from images at 5.5 and 1.5-arcsec resolution, and from CLEAN and maximum-entropy images at the higher resolution, showed differences at the level of $\Delta\alpha \gtrsim 0.1$ farther from the nucleus.
- (iii) In order to keep the rms error in fitted spectral in-

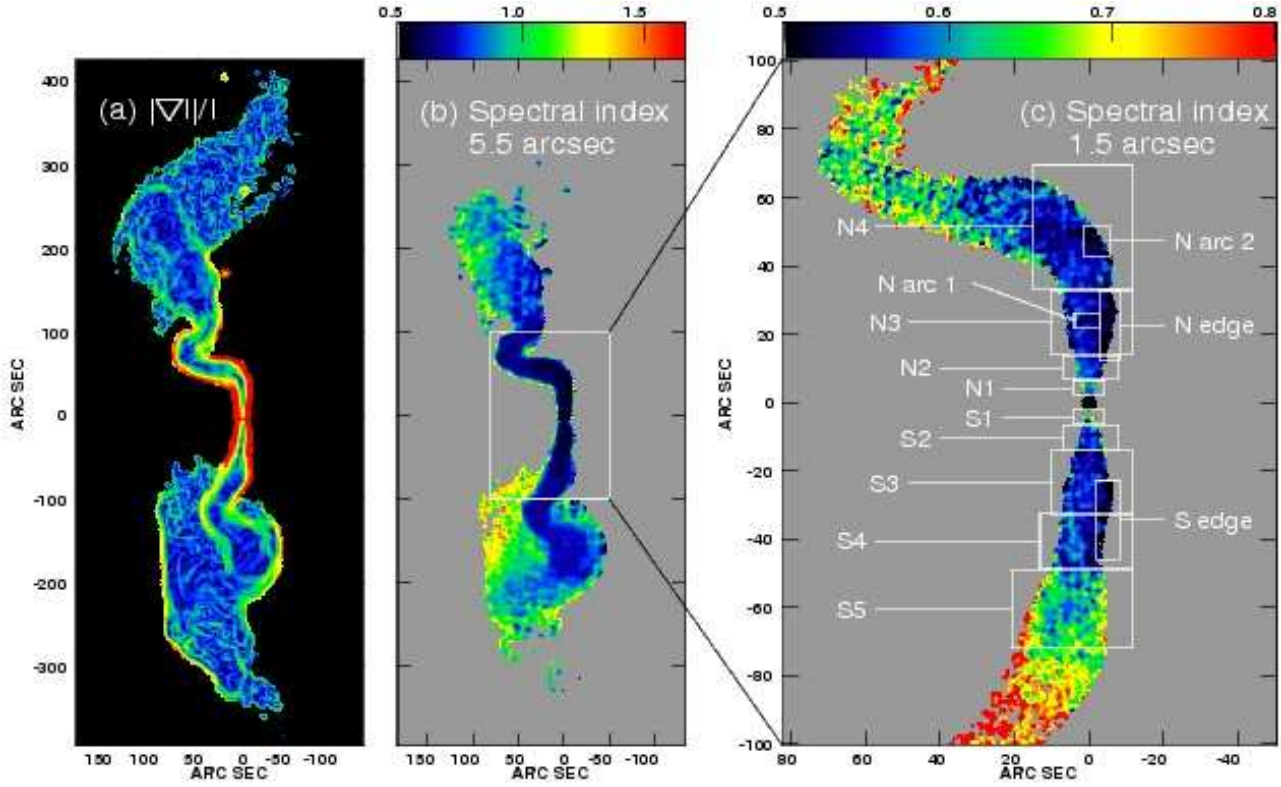


Figure 12. (a) Sobel-filtered, mean L-band image (Section 2.2), normalized by total intensity, at a resolution of 5.5 arcsec. (b) and (c) Spectral index, α from weighted least-squares, power-law fits to the total intensity. (b) 5-frequency fit between 1365 and 4985 MHz at a resolution of 5.5 arcsec FWHM. Only points with $I > 5\sigma$ at all frequencies are shown. The colour range is $0.5 \leq \alpha \leq 1.66$. (c) 6-frequency fit to the maximum-entropy images at a resolution of 1.5 arcsec FWHM for the inset area in panel (b). Only points with $I > 10\sigma$ at all frequencies were used in the fit. The colour range is $0.5 \leq \alpha \leq 0.8$. The boxes mark the regions used for the fits in Fig. 13 and Table 3. All of the images have been rotated anticlockwise by 19.7 deg.

dex $\lesssim 0.1$ at 1.5-arcsec resolution, we required that all input images had $I > 10\sigma$; this condition was satisfied only in the central regions.

For the same reasons, we can search for deviations from a power-law spectrum only in the inner jets.

Experience suggests that the combination of calibration and deconvolution errors results in an rms $\sigma_I \approx 0.03I$. When fitting spectra, we have therefore added this term and the off-source noise from Table 2 (corrected for primary-beam attenuation) in quadrature. As noted in Section 2.2, chromatic aberration does not affect the measured brightnesses for 3C 31 significantly. The reason is that the effect preserves flux density and 3C 31 is very well resolved on all scales where it is important.

5.2 Power-law spectra

The best representation of the spectrum at a resolution of 5.5 arcsec is given by a weighted least-squares fit of power-law spectra to the I images over the frequency range 1365 – 4985 MHz (Fig. 12b). The ‘spectral tomography’ technique of Katz-Stone & Rudnick (1997) and Katz-Stone et al. (1999) leads to similar conclusions, but our use of all of the available frequencies minimizes noise.

The spectral index variation over the inner jets is shown in more detail in Fig. 12(c), which is derived from a six-

frequency power-law fit at 1.5-arcsec resolution. Points are only plotted if: (a) $I > 10\sigma$ at all frequencies (resulting in a maximum rms error in spectral index of 0.11) and (b) the spectral indices derived from CLEAN and maximum-entropy images differ by < 0.075 . In order to search for deviations from power-law spectra at high signal-to-noise ratio, we have integrated the flux densities over the rectangular regions shown in Fig. 12(c) for the 1.5-arcsec FWHM images, using the same blanking criterion as for the spectral-index map in Fig. 12(c). The results are shown in Fig 13 and the spectral indices are tabulated in Table 3.

5.3 Spectral variations

5.3.1 Description

The principal features of the spectra shown by Figs 12 and 13 are as follows:

(i) There is no evidence for any significant deviation from power-law spectra wherever we have reliable 8440-MHz data (i.e. within 70 arcsec of the nucleus). All of the fits shown in Fig. 13 except for S1 have a probability > 0.45 that the chi-squared statistic would exceed the measured value by chance, suggesting that we have slightly overestimated the multiplicative error term. For S1 (the faint region of the counter-jet close to the core) there are significant residual artefacts at L band which are not represented in our noise

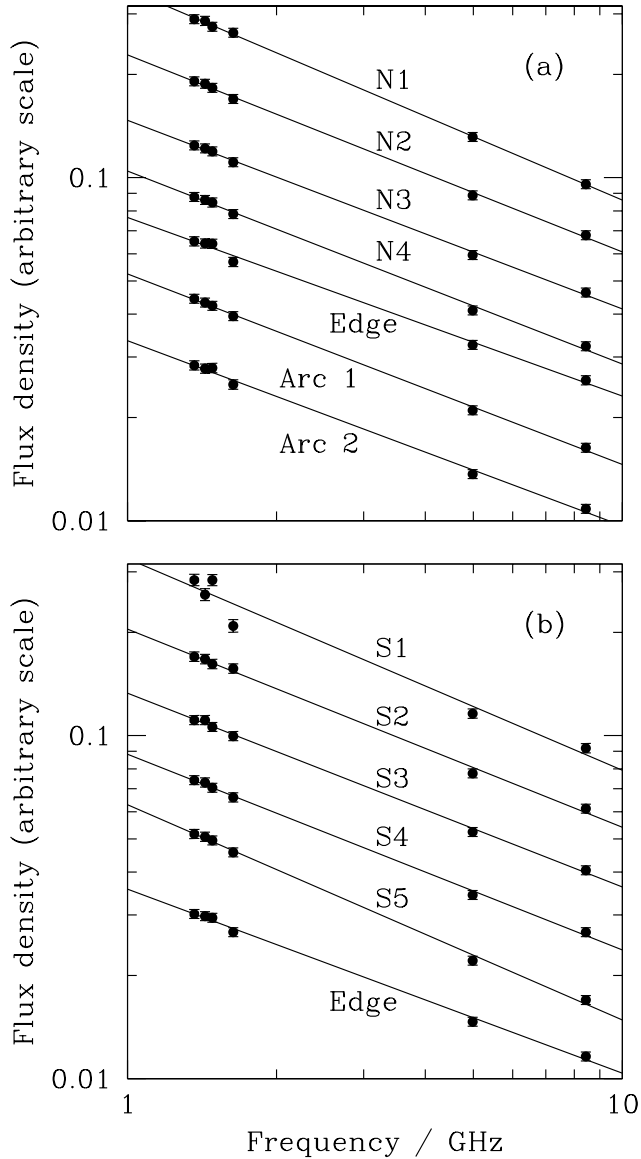


Figure 13. Power-law fits to the total-intensity images over the rectangular regions shown in Fig. 12(c). (a) North jet, (b) South jet.

estimate. Our constraints on spectral curvature are limited by calibration uncertainties at the 1 – 2% level (it is clear from Fig. 13 that the 1636- and 4985-MHz points are slightly low relative to the best-fitting power law and the 8440-MHz points slightly high). In any case, the curvature expected over our restricted frequency range is small, because of the finite width of the synchrotron emission spectrum for a single electron. For these reasons, we will not discuss spectral curvature in what follows. As the calibration differences are common to all of the fits, the differences in spectral index *between regions* are better determined than the absolute values or curvature, however, with an estimated rms error of only 0.01.

(ii) Within ≈ 7 arcsec of the nucleus in both jets, the spectral index at 1.5-arcsec resolution is slightly steeper ($\langle\alpha\rangle = 0.62$) than the average for the inner jets.

(iii) From 7 – 50 arcsec in both jets, the mean spectral

index is in the range 0.55 – 0.57. Farther from the nucleus, there is a gradual spectral steepening.

(iv) There are also slight, but significant variations in spectral index across both jets within ≈ 30 arcsec of the nucleus in the sense that their West edges tend to have flatter spectra ($\langle\alpha\rangle = 0.52 - 0.54$; Fig. 12c). We are confident that this is not an instrumental effect: it is clearly visible at both resolutions and on the CLEAN and maximum-entropy images. Any residual misalignments of the images, particularly at 1.5-arcsec resolution, should be extremely small. The most likely remaining error (confusion with the unresolved radio core at the base of the North jet) would not produce a difference in spectral index across the jets. Flatter spectra are also seen on both edges of the jets in NGC 315 (Laing et al. 2006a).

(v) The spectra of the two brightest arcs in the North jet are also slightly flatter than that of the surrounding emission (Fig. 12c; Table 3).

(vi) There is a clear spectral separation between the South jet and the spur emission, matching the separation of these regions defined by the sharpest brightness gradients (Figs 12a and b). This is particularly clear where the jet first enters the diffuse emission. The spectral identity of the jet is evidently maintained even after it bends abruptly about 2 arcmin South of the nucleus and remains until it terminates in a region of high brightness gradient. The outer South jet in 3C 31 is therefore a clear example of the type of spectral structure noted in other FRI sources (Katz-Stone & Rudnick 1997; Katz-Stone et al. 1999) wherein a flatter-spectrum ‘jet’ with a distinct spectral identity is superposed on steeper-spectrum ‘sheath’ emission.

(vii) There are hints of a similar spectral difference between the jet and the spur and tail in the North, but the sensitivity and short-spacing coverage of the 4985-MHz observations are inadequate to confirm this. The difference is seen clearly in WSRT observations at 0.6 and 1.4 GHz with a resolution of 29×55 arcsec FWHM (fig. 3g of Jägers 1987).

(viii) Approximate subtraction of the steeper-spectrum sheath emission by linear interpolation under the jets shows that there must be some intrinsic steepening of the jet spectrum with increasing distance from the nucleus in addition to the apparent steepening caused by emission from sheath material along the line of sight. The complex morphology of the South spur and tail make it difficult to separate the spectral components unambiguously, however.

(ix) At 5.5-arcsec resolution, the spectral index of the North jet is flatter by 0.1 – 0.2 on-axis than at the edges in the region of the double bend, between 80 and 120 arcsec from the nucleus, the flattest spectrum being associated with a bright filament (Fig. 12b). Similarly, transverse spectral gradients in the opposite sense to those described in (iv) – i.e. with the jet spectrum flatter on-axis – are seen at distances $\gtrsim 50$ arcsec from the nucleus at 1.5-arcsec resolution (Fig. 12c). These effects are most likely to be produced by blending of flat-spectrum emission from the jets with steep-spectrum emission from the surrounding spurs and tails.

(x) Andernach et al. (1992) found that within 9 arcmin of the core the spectrum observed with low resolution flattens above 5 GHz, as previously suspected by Burch (1977). They interpreted this effect as a superposition of components with

Table 3. Spectral indices from 6-frequency power-law fits for the regions shown in Fig. 12(c). The flux densities used in the fits were derived by integration over the images at 1.5-arcsec resolution. The rms errors on the spectral indices are all between 0.017 and 0.020, and are dominated by calibration uncertainties. The rms errors on spectral-index differences between regions are ≈ 0.01 .

| Region | α |
|---------|----------|
| N arc 2 | 0.54 |
| N arc 1 | 0.56 |
| N edge | 0.52 |
| N4 | 0.56 |
| N3 | 0.55 |
| N2 | 0.58 |
| N1 | 0.62 |
| S1 | 0.62 |
| S2 | 0.58 |
| S3 | 0.57 |
| S4 | 0.57 |
| S5 | 0.63 |
| S edge | 0.54 |

different spectra, a conclusion which is confirmed directly by our data.

5.3.2 Spectral variations in FRI jets

These observations contribute to the developing picture of spectral variations in the bases of FRI jets, as follows.

(i) Where the jets first brighten, there is a remarkably small dispersion around a spectral index of $\alpha = 0.62$ in the three sources we have studied in detail: 3C 31, NGC 315 (Laing et al. 2006a) and 3C 296 (Laing et al. 2006b), as well as 3C 66B (Hardcastle et al. 2001). The average is dominated by emission immediately after the brightening point (Fig. 6).

(ii) The spectral index of the fainter emission close to the nucleus in 3C 449 (Rudnick & Katz-Stone 1997), PKS1333–33 (Killeen et al. 1986) and 3C 66B (Hardcastle et al. 2001) appears to be comparable or slightly steeper although the uncertainties are larger. We do not have adequate resolution to measure the spectral index in these parts of the jets in 3C 31.

(iii) Farther from the nucleus, the radio spectra flatten slightly to $\alpha = 0.50 - 0.55$. This flattening occurs where our kinematic models require deceleration (Laing & Bridle 2002a; Canvin et al. 2005; Laing et al. 2006b).

(iv) A related result is that an asymptotic low-frequency spectral index of 0.55 is common in FRI jets over larger areas than we consider here (Young et al. 2005).

(v) Flatter-spectrum edges can be seen where the jets are isolated from significant surrounding diffuse emission. Our kinematic models (Laing & Bridle 2002a; Canvin et al. 2005; Laing et al. 2006b) show that all of the jets have substantial transverse velocity gradients in these regions.

(vi) Our kinematic models and spectral measurements together suggest a relation between spectral index and flow speed $\beta = v/c$, ranging from $\alpha = 0.62$ for $\beta \approx 0.8$ to $\alpha \approx 0.5$ for $\beta \lesssim 0.2$. Spectra would then be expected to flatten with

distance from the nucleus (as the jets decelerate) and from centre to edge (as a result of transverse velocity gradients).

(vii) Synchrotron X-ray emission from the main jets in 3C 66B, 3C 31, 3C 296 and NGC 315 is strongest relative to the radio close to the nucleus, at or before the brightening point (Hardcastle et al. 2001, 2002, 2005; Worrall et al. 2007). X-ray emission is still detected from the flatter-spectrum regions farther out, but at a lower level relative to the radio.

(viii) There is approximate morphological correspondence between the radio and X-ray brightness distributions, but they differ in detail. In the best-resolved case, NGC 315 (Worrall et al. 2007), the X-ray emission is clearly extended across the jet. Particle acceleration appears to be distributed throughout the jet volume, rather than being exclusively associated with discrete knots or with the boundary.

(ix) The ratio of X-ray to radio emission decreases and the radio spectrum starts to flatten where our kinematic models show that the jets decelerate rapidly from speeds of $\beta \approx 0.8 - 0.9$ (Laing & Bridle 2002a; Hardcastle et al. 2002; Canvin et al. 2005; Worrall et al. 2007).

(x) The strongest X-ray emission is not associated with the flattest radio spectra, but rather with some particle acceleration process whose characteristic energy index is $s = 2\alpha + 1 = 2.24$. This is intriguingly close to the asymptotic value of $s = 2.23$ for first-order Fermi acceleration at relativistic shocks in the limit of large shock (or, equivalently, upstream) Lorentz factor Γ , a result which holds even for relativistically hot jets (Kirk et al. 2000 and references therein; Kirk 2005). The asymptotic value of s is only approached for $\Gamma = (1 - \beta^2)^{-1/2} \gtrsim 10$ (Kirk et al. 2000; Lemoine & Pelletier 2003), however, so we would have to suppose that some fraction of the flow before the brightening point has a bulk Lorentz factor $\Gamma \gtrsim 10$ and decelerates to $\Gamma \approx 2$, as required by our kinematic models. The shock would then have to be oblique, since the normal component of the the incoming plasma speed would be reduced to $\beta \approx 1/3$ at the shock. Such a flow would be difficult to detect because of the narrow beaming angle, even if it contains relativistic particles. Emission before the brightening point would then come primarily from a slow surface layer, as suggested for 3C 31 by Laing & Bridle (2002a).

(xi) As the jet slows down and the shocks become both less relativistic and weaker, the energy index would decrease, eventually reaching $s = 2$ ($\alpha = 0.5$) when the shocks become non-relativistic (Bell 1978). Although this provides a natural reason for the spectrum of a jet to flatten as it decelerates, the required flow speeds are higher than we infer. In particular, the spectral index of $\alpha = 0.61$ is seen over a distance of ≈ 8 kpc (corrected for projection) along the jet axis in NGC 315, in a region where we infer the on-axis flow to have $\Gamma \approx 2.1$ (Canvin et al. 2005; Laing et al. 2006a). We would then have to suppose that some part of the flow remains ultrarelativistic (and effectively invisible) on large scales.

(xii) A second possibility is that the process that produces the flatter spectrum is associated with shear (Laing et al. 2006a). In 3C 31, flatter-spectrum edges occur predominantly on the Western edges of the jets, i.e. on the outer edges of bends, perhaps consistent with this idea. Second-order Fermi acceleration driven by turbulence in the shear layer (Stawarz & Ostrowski 2002) appears to be a viable

process in FRI jets, but the shear acceleration mechanism described by Rieger & Duffy (2004) is unlikely to be efficient enough to accelerate the X-ray-emitting electrons in the relatively modest velocity gradients we infer.

(xiii) The idea that two different acceleration processes are required has also been suggested on the basis of evidence from the X-ray morphology and spectrum of the brighter jet in Cen A (Kataoka et al. 2006; Hardcastle et al. 2007). Here, the compact knots observed close to the nucleus are thought to be associated with shocks, while a truly diffuse acceleration mechanism dominates at larger distances.

Far from the nucleus, the picture is complicated by the presence of diffuse emission surrounding the jets. As well as a smooth steepening of the jet spectrum (expected from synchrotron and adiabatic losses affecting a homogeneous electron population), multiple spectral components are observed. Jets appear to retain their identities even after entering regions of diffuse emission and are clearly identifiable by their flatter spectra. They are usually separated from the surrounding emission by sharp brightness gradients. This separation is observed in FRI sources with bridges of emission extending back towards the nucleus (e.g. 3C 296; Laing et al. 2006b) as well as sources with tails and spurs like 3C 31. Although there is an overall trend for the spectrum of the diffuse emission to steepen towards the nucleus in bridges and away from it in tails (Parma et al. 1999), the variations in individual objects such as 3C 31 are complex. The termination regions of jets in tailed FRI sources are perhaps best regarded as bubbles which are continually fed with fresh relativistic plasma by the jets and which in turn leak material into the tails. Their spectral steepening would then be governed by a combination of continuous injection, adiabatic, synchrotron and inverse Compton energy losses and escape.

6 SUMMARY AND CONCLUSIONS

Our new images of the FRI radio galaxy 3C 31 reveal a complex substructure of arcs and filaments within the jets and tails that is clearly related to the organization of the apparent magnetic field structure. There is a strong correspondence between steep brightness gradients and the organization of the apparent field direction perpendicular to such gradients.

Laing & Bridle (2002a) have shown that the detailed brightness and polarization properties of the inner jets in 3C 31 are consistent with interpreting them as intrinsically symmetrical relativistic flows that decelerate with increasing distance from the nucleus, so that the observed asymmetries also decline with distance. We suggest that the observed differences between the intensity and polarization structures of the arcs in the inner main and counter-jets are also caused by the effects of aberration on emission from intrinsically similar structures.

Our new data further suggest that we are observing the transition between predominantly relativistic asymmetries which dominate in the straight inner parts of the main jet and the counter-jet and environmental asymmetries which dictate the appearance of 3C 31 at distances $\gtrsim 1$ arcmin from the nucleus. Effects of an asymmetric environment include: (a) the different scales on which bending begins in the North

and South jets; (b) the dissimilar morphologies of the North and South spurs and tails, and (c) the lack of any systematic correspondence between the locations, shapes and brightnesses of substructures in the outer parts of the North and South jets.

Our images also show that both jets in 3C 31 retain their spectral identity far from the galactic nucleus, where their emission is superimposed on larger-scale, steeper- spectrum structures. Spectral imaging and intensity-gradient imaging (Sobel filtering) techniques both delineate the *same* boundaries between the jets and their environs on both the North and South sides of the galaxy.

The radio spectra of the inner jets of 3C 31 and other FRI radio galaxies exhibit systematic trends which are related both to jet kinematics and to X-ray emission:

(i) The characteristic radio spectral index where the jets first brighten is $\alpha = 0.62 \pm 0.01$. The ratio of X-ray/radio emission is highest at and before the brightening point.

(ii) Farther out, the spectrum flattens slightly, to $\alpha \approx 0.50 - 0.55$ and the X-ray emission is fainter relative to the radio. The onset of this spectral flattening coincides with deceleration of the flow in our kinematic models.

(iii) Flatter spectra are seen at the jet edges where the jets are isolated from significant diffuse emission, in regions where our kinematic models require significant transverse velocity gradients.

The correlation between radio spectral index and X-ray emission suggests a direct association with the particle-acceleration process. The energy index of 2.24 corresponding to $\alpha = 0.62$ is close to the asymptotic value for relativistic shocks in the limit of high Lorentz factors, and the spectral flattening could result from progressive weakening of the shocks as the jets slow down. The Lorentz factors of at least some parts of the flow would have to be much higher than we infer, however. Alternatively, there may be two different acceleration mechanisms operating on kpc scales in these jets, one dominant from the nucleus until the region where jets brighten abruptly in the radio, the other taking over at larger distances and perhaps associated with transverse velocity shear.

ACKNOWLEDGEMENTS

RAL would like to thank the Istituto di Radioastronomia, NRAO and Alan and Mary Bridle for hospitality during the course of this work. We acknowledge travel support from NATO Grant CRG931498. We thank John Kirk for advice on particle acceleration mechanisms and the referee, John Wardle, for his helpful report. The National Radio Astronomy Observatory is a facility of the National Science Foundation operated under cooperative agreement by Associated Universities, Inc.

REFERENCES

- Andernach, H., Feretti, L., Giovannini, G., Klein, U., Rossetti, E., Schnaubelt, J., 1992, A&AS, 93, 331
- Arp, H., 1966, ApJS, 14, 1
- Bell, A.R., 1978, MNRAS, 182, 147

- Burch, S.F., 1977, MNRAS, 181, 599
- Burch, S.F., 1979, MNRAS, 187, 187
- Butcher, H.R., van Breugel, W.J.M., Miley, G.K., 1980, ApJ, 235, 749
- Canvin, J.R., Laing, R.A., Bridle, A.H., Cotton, W.D., 2005, MNRAS, 363, 1223
- Croston, J.H., Birkinshaw, M., Conway, E., Davies, R.L., 2003, MNRAS, 339, 82
- de Koff, S., Best, P., Baum, S. A., Sparks, W., Röttgering, H., Miley, G., Golombek, D., Macchetto, F., Martel, A., 2000, ApJS, 129, 33
- De Vaucouleurs, G., De Vaucouleurs, A., Corwin, H.G. Jr., Buta, R., Paturel, G., Fouque, P., 1991, Third Reference Catalogue of Bright Galaxies, Springer-Verlag, New York
- Fanaroff, B.L., Riley, J.M., 1974, MNRAS, 167, 31P
- Fomalont, E. B., Bridle, A. H., Willis, A.G., Perley, R. A., 1980, ApJ, 237, 418
- Fraix-Burnet, D., Golombek, D., Macchetto, F., 1991, AJ, 102, 562
- Hardcastle, M.J., Birkinshaw, M., Worrall, D.M., 2001, MNRAS, 326, 1499
- Hardcastle, M.J., Worrall, D.M., Birkinshaw, M., Laing, R.A., Bridle, A.H., 2002, MNRAS, 334, 182
- Hardcastle M.J., Worrall D.M., Birkinshaw M., Laing R.A., Bridle A.H., 2005, MNRAS, 358, 843
- Hardcastle M.J., et al., 2007, ApJ, 670, L81
- Huchra, J.P., Vogeley, M.S., Geller, M.J., 1999, ApJS, 121, 287
- Jägers, W.J.M., 1987, A&AS, 71, 75
- Kataoka, J., Stawarz, L., Aharonian, F., Takahara, F., Ostrowski, M., Edwards, P.G., 2006, ApJ, 641, 158
- Katz-Stone, D.M., Rudnick, L., 1997, ApJ, 488, 146
- Katz-Stone, D.M., Rudnick, L., Butenheoff, C., O'Donoghue, A.A., 1999, ApJ, 516, 716
- Keel, W.C., 1988, ApJ, 329, 532
- Killeen N.E.B., Bicknell G.V., Ekers R.D., 1986, ApJ, 302, 306
- Kirk, J.G., 2005, in Chen P., Bloom E., Madejski G., eds, 22nd Texas Symposium on Relativistic Astrophysics, at Stanford. SLAC, Stanford, <http://www.slac.stanford.edu/econf/C041213/>
- Kirk, J.G., Guthman, A.W., Gallant, Y.A., Achterberg, A., 2000, ApJ, 542, 235
- Komossa, S., Böhringer, H., 1999, A&A, 344, 755
- Laing, R.A., 1980, MNRAS, 193, 439
- Laing, R.A., 1981, ApJ, 248, 87
- Laing, R.A., Bridle, A.H., 2002a, MNRAS, 336, 328
- Laing, R.A., Bridle, A.H., 2002b, MNRAS, 336, 1161
- Laing, R.A., Bridle, A.H., 2004, MNRAS, 348, 1459
- Laing, R.A., Bridle, A.H., Parma, P., Murgia, M., 2008, MNRAS, submitted
- Laing, R.A., Canvin, J.R., Cotton, W.D., Bridle, A.H., 2006a, MNRAS, 368, 48
- Laing, R.A., Canvin, J.R., Bridle, A.H., Hardcastle, M.J., 2006b, MNRAS, 372, 510
- Lara, L., Cotton, W.D., Feretti, L., Giovannini, G., Venturi, T., Marcaide, J.M., 1997, ApJ, 474, 179
- Lemoine, M., Pelletier, G., 2003, ApJ, 589, L73
- Martel, A., Baum, S. A., Sparks, W. B., Wyckoff, E., Biretta, J. A., Golombek, D., Macchetto, F. D., de Koff, S., McCarthy, P. J., Miley, G. K., 1999, ApJS, 122, 81
- Okuda, T., Kohno, K., Iguchi, S., Nakanishi, K., 2005, ApJ, 620, 673
- Parma, P., Murgia, M., Morganti, R., Capetti, A., de Ruiter, H.R., Fanti, R., 1999, A&A, 344, 7
- Pratt, W.K., 1991, Digital Image Processing, Wiley, New York
- Rieger F.M., Duffy P., 2004, ApJ, 617, 155
- Rudnick, L., Katz-Stone, D.M., 1997, ApJ, 488, 146
- Smith, R.J., Lucey, J.R., Hudson, M.J., Schlegel, D.J., Davies, R.L., 2000, MNRAS, 313, 469
- Stawarz, L., Ostrowski, M., 2002, ApJ, 578, 763
- Strom, R.G., Fanti, R., Parma, P., Ekers, R.D., 1983, A&A, 122, 305
- Taylor, G. B., Ulvestad, J.S., Perley, R.A., The Very Large Array Observational Status Summary, NRAO, Socorro, URL: <http://www.vla.nrao.edu/astro/guides/vlas/current/>
- Wardle, J.F.C., Kronberg, P.P., 1974, ApJ, 194, 249
- Worrall D.M., Birkinshaw M., Laing, R.A., Cotton, W.D., Bridle, A.H., 2007, MNRAS, 380, 2
- Young A., Rudnick L., Katz D., Delaney T., Kassim N.E., Makishima K., 2005, ApJ, 626, 748
- Zwicky, F., Kowal. C. T., 1968, Catalogue of Galaxies and Clusters of Galaxies, Vol.6, California Institute of Technology, Pasadena